Hindawi
Advances in Civil Engineering
Volume 2024, Article ID 2316053, 19 pages
https://doi.org/10.1155/2024/2316053

Research Article

Energy-Balance-Based Plastic Design and Seismic Fragility Analysis of Steel Plate Shear Wall Coupled with Steel Side Columns

Y. T. Wu,[1,2] **Aozhou Liu**,[2] **Jiazheng Zhao**,[2] **and Bo Zhang**[2]

[1]*Department of Civil and Environmental Engineering, University of Houston, Houston, TX 77204, USA*
[2]*School of Civil Engineering, Chongqing University, Chongqing 400044, China*

Correspondence should be addressed to Y. T. Wu; ywu77@uh.edu

Received 4 August 2023; Revised 10 December 2023; Accepted 2 January 2024; Published 29 January 2024

Academic Editor: Edén Bojórquez

The steel plate shear wall (SPSW) coupled with steel side columns (SSCs) through steel coupling beams, or the SPSW–SSC coupled structural system, is a novel lateral force resisting system that introduces coupling mechanism to the isolated SPSW pier. To simplify the complex iteration of the conventional seismic design procedure and obtain the favorable plasticity development and distribution pattern determined by the coupling mechanism, the energy-balance concept and the plastic design method are combined to develop the energy-balance-based plastic design (EBPD) method for the SPSW–SSC coupled system with the consideration of the degradation of hysteretic behavior. Twelve SPSW–SSC coupled system prototype cases with different story numbers and coupling ratios (CRs) were designed and numerically modeled to simulate the main seismic behavior. The pushover analyses and the incremental dynamic analyses were further carried out to examine the lateral load capacity and deformation relationships and the seismic fragility curves with respect to the performance levels quantified by the maximum interstory drift ratios. The analysis results prove that the coupling mechanism can be realized in the SPSW–SSC coupled system with preferred yielding sequence and plasticity distribution mode. The influences of story number and CR on the lateral load capacity curves are revealed. The seismic fragility analysis results indicate the exceeding probability of the limit states corresponding to different performance levels with the consideration of the influences of story number and CR, which further proves the effectiveness of the proposed EBPD methods in terms of the realization of the coupling mechanism and the earthquake collapse safety of the SPSW–SSC coupled structural system.

1. Introduction

The steel plate shear wall (SPSW), consisting of horizontal and vertical boundary elements (HBEs and VBEs) and infill steel plate panels, has been widely constructed as the lateral force resisting system in buildings for its great lateral strength and stiffness, stable hysteretic characteristics, high plastic energy absorption capacity, and superior constructability. The SPSW can be designed to resist the earthquake-induced lateral loads through the full in-plane shear capacity of the stiffened infill plates without out-of-plane buckling [1, 2] or the postbuckling tension field action if thin unstiffened infill plates are used [3–5], depending on different seismic design philosophies. Over the past decades, innovative types of SPSW have been investigated to address some structural issues of conventional SPSWs and achieve better seismic performance. The low-yield point SPSW employs low-yield stress steel plates to improve the buckling stability, energy absorption capacity, and serviceability [6, 7]. The self-centering SPSW uses post-tensioned connections in the boundary frame to provide recentering capability and mitigate frame damages [8]. Infill steel plates with irregular shapes or geometries such as corrugated plates [9] and perforated plates [10] were also developed for improved behavior. However, since the internal bending moment demand at the cross-section of the SPSW reduces with the structural height, the postyield damages concentrate at the bottom regions of the isolated SPSWs, causing difficulty in postquake reparation and inefficient use of materials at the

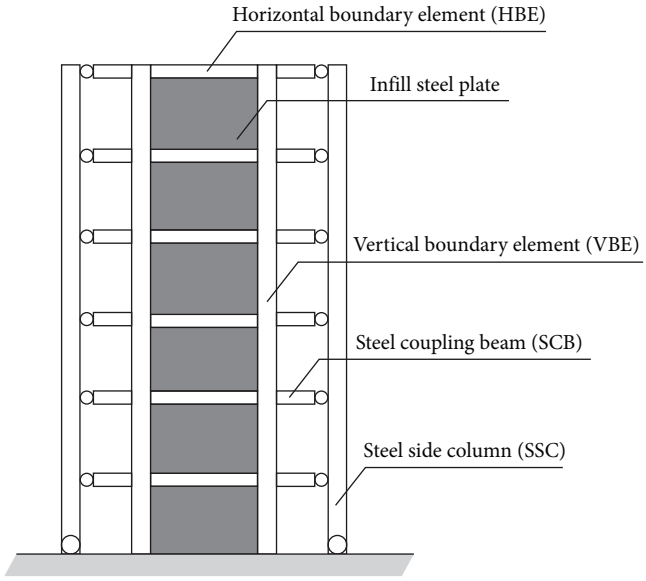

Figure 1: Schematic of SPSW–SSC coupled system.

upper wall portion [11]. In recent years, the coupled SPSW system, where two or more adjacent SPSW piers are joined by steel coupling beams (SCBs) at floor levels, has attracted the attention of researchers. It has been established through experimental and numerical studies that the coupled SPSW system can maintain the ductile and robust seismic performance of isolated SPSWs while significantly improving the material efficiency that isolated SPSWs cannot achieve, thanks to the inherent coupling mechanism of the coupled wall system [12–15]. The benefits and advantages of the coupled mechanism, or the coupling action, over isolated walls have been summarized in the literature [16]. It is without doubt that all the abovementioned previous research has been with respect to the multipier SPSWs joined by SCBs, where the coupling mechanism is realized through the interaction between SCBs and adjacent SPSW piers.

In order to introduce the coupling mechanism in the isolated SPSW, an innovative coupled structural system involving an interior SPSW and two steel side columns (SPSW–SSCs) joined by SCBs was proposed. As shown in Figure 1, the SSCs on both sides of the isolated SPSW are intended to develop axial forces only and form the tension–compression couple to resist a portion of the total overturning moment induced by earthquakes. Shear connections should be assured between the SCBs and the SSCs and at the base of the SSCs so that only shear force and axial force can be transferred. The benefits of such SPSW–SSC coupled structural system are obvious: due to the additional force couple formed between the SSCs, the overturning moment demand at the SPSW bottom section is significantly reduced; the SCBs can yield and consume most of the earthquake-induced energy through considerable plastic shear rotations prior to the formation of plastic hinge at the SPSW bottom region; and the entire height of the SPSW can be uniformly mobilized to provide post-yield mechanical and deformation capacities. Although previous research has numerically proved similar coupled systems consisting of reinforced concrete walls and SSCs connected with steel links can be proportioned to exhibit the preferred yield sequence and failure pattern [17–19], research on SPSW–SSC coupled system has rarely been reported. Behavior of the SPSW is more complicated than RC walls in that the interaction between the boundary frame members (HBE and VBE) and the infill web plates has a significant impact on the overall behavior of the SPSW [14]. Research efforts in developing rational seismic design method and examining the seismic behavior of the SPSW–SSC coupled system are needed.

In this research program, energy-balance-based plastic design (EBPD) method for the SPSW–SSC coupled system was developed based on previous research on energy-based seismic design methods [20, 21] and performance-based plastic design methods [22–24]. By introducing the EBPD method, the preferred plasticity development and distribution pattern resulted from the coupling mechanism can be reflected in the early design stage; the total base shear of the coupled system can be directly and reasonably computed even though this innovative structural system has not been included in current building codes [25]. The elastic and perfectly plastic force–displacement (EPP *F–D*) behavior for multiple degree of freedom (MDOF) system is assumed in the EBPD method, which is very suitable to the SPSW–SSC system. To further investigate the behavior of the proposed SPSW–SSC coupled system, 12 prototype SPSW–SSC coupled systems with different heights and coupling ratios (CRs) were designed and modeled with numerical techniques verified against experimental results from the available literature. Then, pushover analyses and seismic fragility analyses using incremental dynamic analyses (IDA) were conducted to reveal the overall seismic performance of the SPSW–SSC coupled system.

2. EBPD Method for SPSW–SSC Coupled System

2.1. Performance Objectives. The ideal failure mode of the SPSW–SSC coupled system is governed by the coupling mechanism that allows the SCBs to fully yield and develop considerable inelastic postyield deformation prior to the significant development of plasticity in the SPSW. The lateral loading conditions and the preferred ultimate yielding conditions are depicted in Figure 2. For the SPSW, the "strong column-weak beam mechanism" is still maintained for the boundary elements in addition to the postbuckling yielding of the tension field strips in the unstiffened infill thin plates. The ultimate lateral deformation of the coupled structural system can be quantified by θ_u, the target maximum interstory drift ratio corresponding to the total lateral displacement at the roof Δ_u. According to the relevant Chinese code [26], the performance objectives of the SPSW–SSC system can be described as follows: θ_u can be 1/200 under moderate earthquakes with reparable damages while 1/50 under rare earthquakes with structural collapse prevented.

2.2. Seismic Design Base Shear. Based on the energy-balance concept shown in Figure 3, the external work that is done by

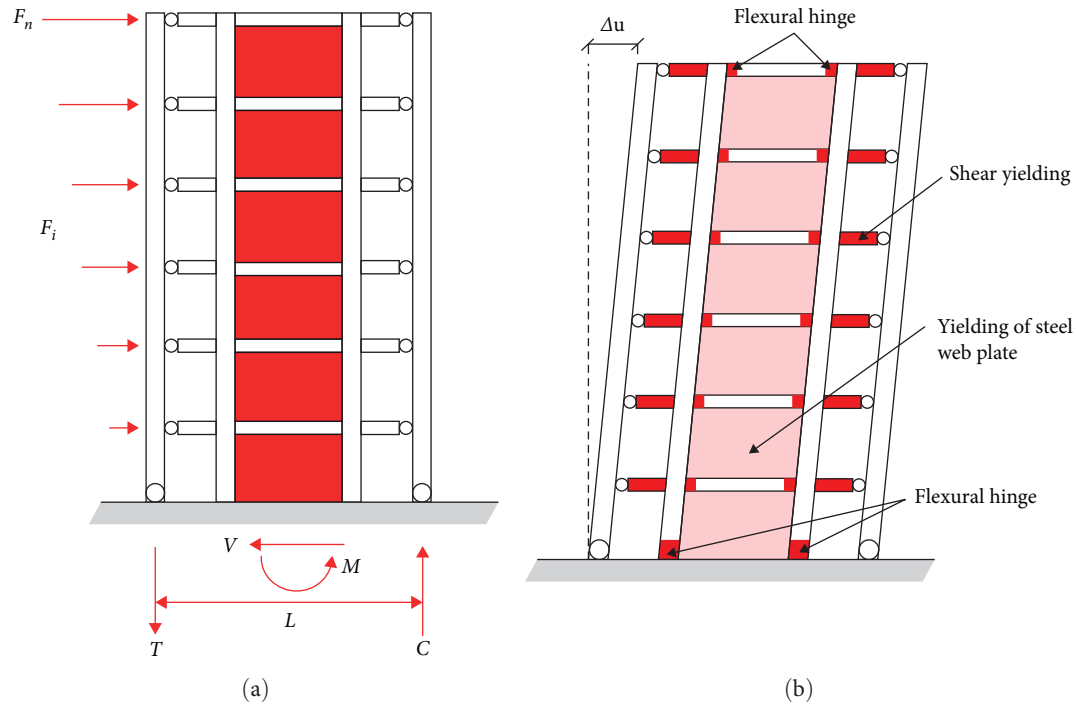

FIGURE 2: Mechanism of SPSW–SSC coupled system: (a) loading condition and (b) preferred ultimate yield mechanism.

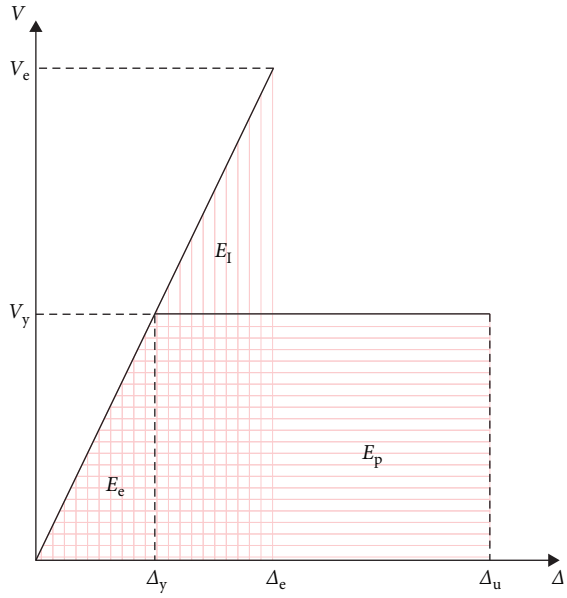

FIGURE 3: Illustration of energy-balance concept.

pushing the structure up to the target interstory drift ratio θ_u is equal to the total energy developed within the structure. Considering appropriate modifications, the energy-balance equation can be written as follows:

$$E_e + \eta E_p = \gamma E_I , \tag{1}$$

where E_e and E_p are the elastic and plastic strain energy developed within the structure, respectively, E_I is the total input earthquake energy, η is the hysteretic energy reduction factor used to account for the difference between the stable and reduced hysteretic loops, and γ is the energy modification factor defined as the ratio of the energy absorbed by an inelastic system to an equivalent elastic system. The relationship between the energy modification factor γ, the displacement ductility factor μ, and the ductility reduction factor R_μ can be expressed by Equation (2):

$$\gamma = \frac{2\mu - 1}{R_\mu^2}, \tag{2}$$

where $\mu = \Delta_u/\Delta y$; $R_\mu = \Delta_e/\Delta_y$; Δ_u and Δ_y are the design ultimate and yield displacements; and Δ_e is the elastic target displacement.

The calculation of E_I is based on the elastic multi-degree-of-freedom (MDOF) system with elastic force–deformation relationship, as shown in Figure 4. V_e and Δ_e are the maximum elastic base shear and the corresponding lateral displacement at the roof of the MDOF system. m_i and k_i are the mass and stiffness of the ith story. The MDOF system is decomposed into a series of elastic single-degree-of-freedom (SDOF) modes. M_i and K_i are the modal mass and stiffness of the ith mode elastic SDOF system. E_I can be calculated by Equation (3):

$$E_I = \sum_{i=1}^{N} \frac{1}{2} M_i^* S_{v,i}^2 = \sum_{i=1}^{N} \frac{1}{2} M_i^* \left(\frac{S_{a,i} T_i}{2\pi} \right)^2 , \tag{3}$$

where M_i^*, $S_{v,i}$, $S_{a,i}$, and T_i are the effective modal mass, the spectra velocity, the spectra acceleration, and the period corresponding to the ith mode elastic SDOF system, respectively.

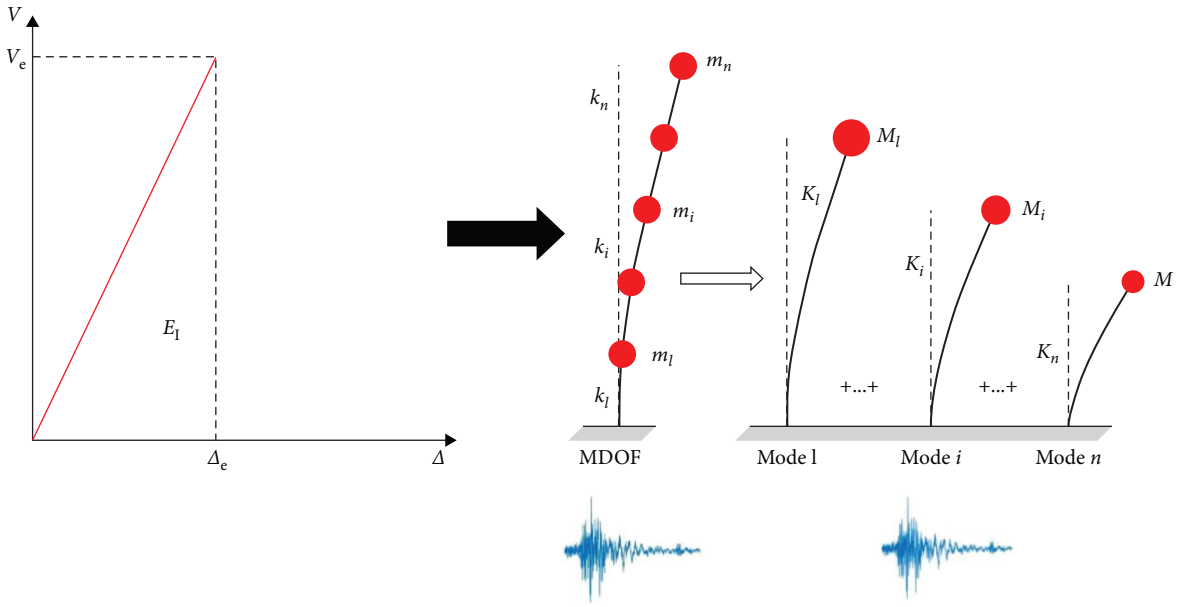

Figure 4: Elastic V–Δ relationship.

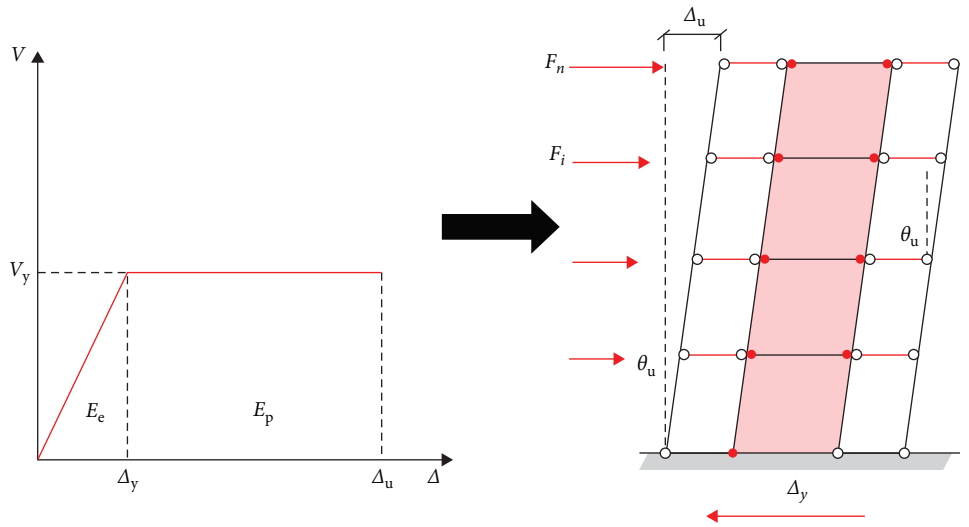

Figure 5: Elasto-perfect plastic (EPP) V–Δ relationship.

To calculate E_e and E_p, the structure is assumed to be an elasto-perfect plastic (EPP) system, as depicted in Figure 5. E_e can be calculated as follows:

$$E_e = \frac{1}{2}\Delta_y \cdot V_y = \frac{1}{2}M \cdot \left(\frac{T}{2\pi} \cdot \frac{V_y}{G} \cdot g\right)^2, \quad (4)$$

where V_y and Δ_y are the design base shear and the corresponding lateral displacement at the roof, M and G are the total mass and seismic weight of the structure, and T is the fundamental period of the structure. To reflect the lateral force distribution pattern corresponding to the plastic state of the structure, the lateral force applied to each floor can be calculated by Equation (5) [27]:

$$F_i = \lambda_i \cdot V_y = (\beta_i - \beta_{i+1}) \left(\frac{G_n h_n}{\sum_{j=1}^{n} G_j h_j}\right)^{0.75T^{-0.2}} \cdot V_y, \quad (5)$$

where F_i is the lateral force of the ith floor, λ_i is the lateral force distribution coefficient, G_j and G_n are the seismic weight concentrated at the jth floor and the roof of the structure, respectively, h_j and h_n are the heights measured from the ground to the jth floor and to the roof level, respectively, β_i is the story shear distribution factor corresponding to the ith story and can be calculated by the following equation:

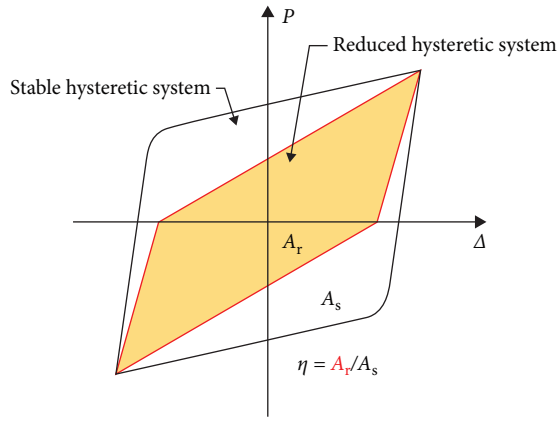

FIGURE 6: Difference of hysteretic loops between stable and reduced system.

$$\beta_i = \frac{V_i}{V_n} = \left(\sum_{j=1}^{n} G_j h_j / G_n h_n\right)^{0.75T^{-0.2}}, \tag{6}$$

where V_i and V_n are the story shears of the ith story and the top story. The plastic strain energy E_P is equal to the work done by the lateral forces after the structure yields, which can be computed by the following equation:

$$E_p = \sum F_i h_i \theta_p = V_y(\theta_u - \theta_y)\sum \lambda_i h_i, \tag{7}$$

where θ_p is the target plastic drift ratio, θ_u is the ultimate drift ratio, θ_y is the interstory drift ratio at yielding and can be 1/250 as suggested by Park et al. [28].

The hysteretic energy reduction factor η in Equation (1) was introduced to account for the variation of the hysteretic loops due to stiffness degradation and strength deterioration during reversed cyclic lateral deformation of a structure. As shown in Figure 6, A_s and A_r are the areas enclosed by hysteretic loop without degradation and hysteretic loop with degradation, respectively. η can be expressed by Equation (8):

$$\eta = \frac{A_r}{A_s}. \tag{8}$$

Although sophisticated methods have been developed to determine the values of η for structural systems with various hysteretic characteristics [29, 30], recent research suggested that the hysteretic energy reduction factor η can be taken as 0.75 for SPSW systems [31].

Inserting Equations (4) and (7) into Equation (1), the design base shear can be calculated as follows:

$$V_y = \frac{2M\theta_p\pi^2\sum_{i=1}^{n}\lambda_i h_i}{T^2} + \sqrt{\left(\frac{2M\theta_p\pi^2\sum_{i=1}^{n}\lambda_i h_i}{T^2}\right)^2 + \frac{4\pi^2 M\gamma E_I}{T^2\eta}}. \tag{9}$$

After taking into account, the effect of gravity on the structure during lateral deformation, the lateral force applied to each floor F_i^D can be calculated as follows:

$$F_i^D = \lambda_i V_y + G_i\theta_u. \tag{10}$$

Then, the total overturning moment M_{OTM} can be calculated as follows:

$$M_{OTM} = \sum_{i=1}^{n} F_i^D h_i. \tag{11}$$

2.3. Design of SCBs and SSCs. The degree of the coupling action can be assessed by the CR for the SPSW–SCC coupled system, which is defined as the ratio of the overturning moment resistance provided by the tension–compression force couple developed between the side columns to the total overturning moment resistance of the system and can be expressed by the following equation:

$$CR = \frac{M_C}{M_{OTM}} = \frac{M_C}{M_C + M_{SPSW}}, \tag{12}$$

where M_C is the tension–compression couple provided by the SSCs, M_{SPSW} is the overturning moment carried by the bottom section of the SPSW, including the contributions of VBEs and infill plate. It is noted that CR is a variable during the loading procedure. For design purposes, the CR corresponding to ultimate yielding condition is adopted to indicate the ultimate plasticity distribution of the structure. The SCBs, similar to the link beams in eccentric moment frames, can be proportioned to be shear dominant to achieve best plastic rotational capacity [31]. Once the total overturning moment of the structure M_{OTM} is determined, the force couple provided by the coupling action can be obtained by the following equation:

$$M_c = M_{OTM} \cdot CR = N_C L_t = \sum_{i=1}^{n} V_{SCB,i} L_t, \tag{13}$$

where N_c is the axial force in SSCs, L_t is the distance between the centerlines of the SSCs, $V_{SCB,i}$ is the plastic shear capacity of the SCB at the ith floor. Shear demands among SCB at different floors are not necessarily uniformly distributed. To improve the material efficiency, the design shear of SCBs can be calculated as follows:

$$V_{SCB,i}^D = \frac{\psi_i}{\sum_{i=1}^{n}\psi_i} \cdot \sum_{i=1}^{n} V_{SCB,i}, \tag{14}$$

where $V_{link,i}^D$ is the design shear of SCB at the ith floor, ψ_i is the shear distribution factor for the SCB at the ith floor. Determination of ψ_i can be complicated in that it depends on value of CR and location of the SCB. The higher the CR, the more shear the SCB at lower stories will resist. However, SCBs are highly ductile elements and force redistribution up to 20% is allowed [32]. If high CR values are used, the story shear distribution factor β_i can be adopted for ψ_i to result in a triangular distribution of shear demands for SCBs [16]. Elastic design method is adopted for the SSC since it is a

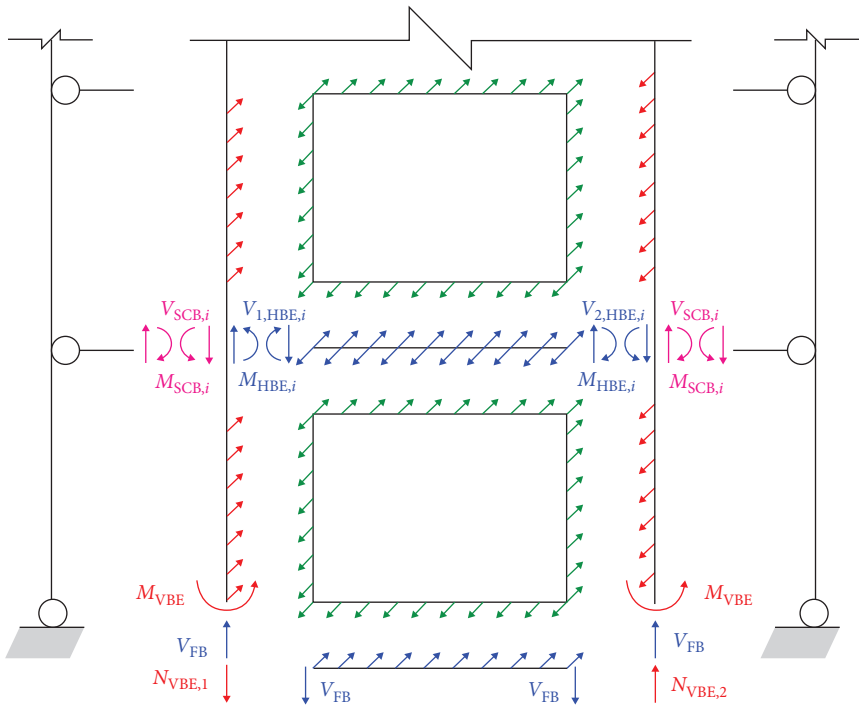

FIGURE 7: Diagram for SPSW design.

non-energy dissipation member. The design axial force can be calculated as follows:

$$N_C^D = 1.1\, r_{OV} \sum_{i=1}^{n} V_{SCB,i}, \tag{15}$$

where N_C^D and R_{OV} are the design axial force and the overstrength factor of SSCs, respectively.

2.4. Design of SPSW. The design of SPSW is based on the plastic analysis that assumes the tension fields form at web plates and plastic hinges develop at the ends of HBE, as depicted in Figure 7. The overturning moment resistance of the SPSW M_W can be expressed by the following equation:

$$M_W = 2M_{VBE} + M_{Pier}\,, \tag{16}$$

$$M_{Pier} = L_W\left(N_{VBE,1} + N_{VBE,2}\right)/2\,, \tag{17}$$

where M_{VBE} is the bending moment at the bottom section of VBE, M_{Pier} is the force couple formed by the tension and compression forces developed at VBE, L_W is the distance between the centroids of the VBE, $N_{VBE,1}$ and $N_{VBE,2}$ are the axial forces developed at VBE. Considering the contribution of the tension fields formed at the web plates, the axial forced developed at VBE can be computed by the following equation:

$$N_{VBE,1} = \sum_{i=1}^{n} \frac{1}{2} F_y H_i t_i \sin 2\alpha_i + \sum_{i=1}^{n} V_{1,HBE,i} - V_{FB} - \sum_{i=1}^{n} V_{SCB,i}, \tag{18}$$

$$N_{VBE,2} = \sum_{i=1}^{n} \frac{1}{2} F_y H_i t_i \sin 2\alpha_i + \sum_{i=1}^{n} V_{2,HBE,i} + V_{FB} - \sum_{i=1}^{n} V_{SCB,i}, \tag{19}$$

where F_y is the yield strength of web plate material, t_i is the web plate thickness of the ith story, H_i is the height of the ith story, α_i is the inclination angle of the tension field of the web plate at the ith story, $V_{1,HBE,i}$ and $V_{2,HBE,i}$ are the shear forces at the ends of the HBE at the ith floor, and V_{FB} is the shear force transferred from the foundation beam to VBE. The shear forces at the ends of HBE can be calculated by Equations (20) and (21):

$$V_{1,HBE,i} = \frac{1}{L_W}\left(2M_{HBE,i} + \frac{L_W^2}{2} F_y \left(t_{i+1}\cos^2\alpha_{i+1} - t_i\cos^2\alpha_i\right)\right), \tag{20}$$

$$V_{2,HBE,i} = \frac{1}{L_W}\left(2M_{HBE,i} - \frac{L_W^2}{2} F_y \left(t_{i+1}\cos^2\alpha_{i+1} - t_i\cos^2\alpha_i\right)\right), \tag{21}$$

where $M_{HBE,i}$ is the plastic flexural capacity of the HBE at the ith floor. Combining Equations (16)–(21), the overturning moment resistance of the SPSW can be obtained by the following equation:

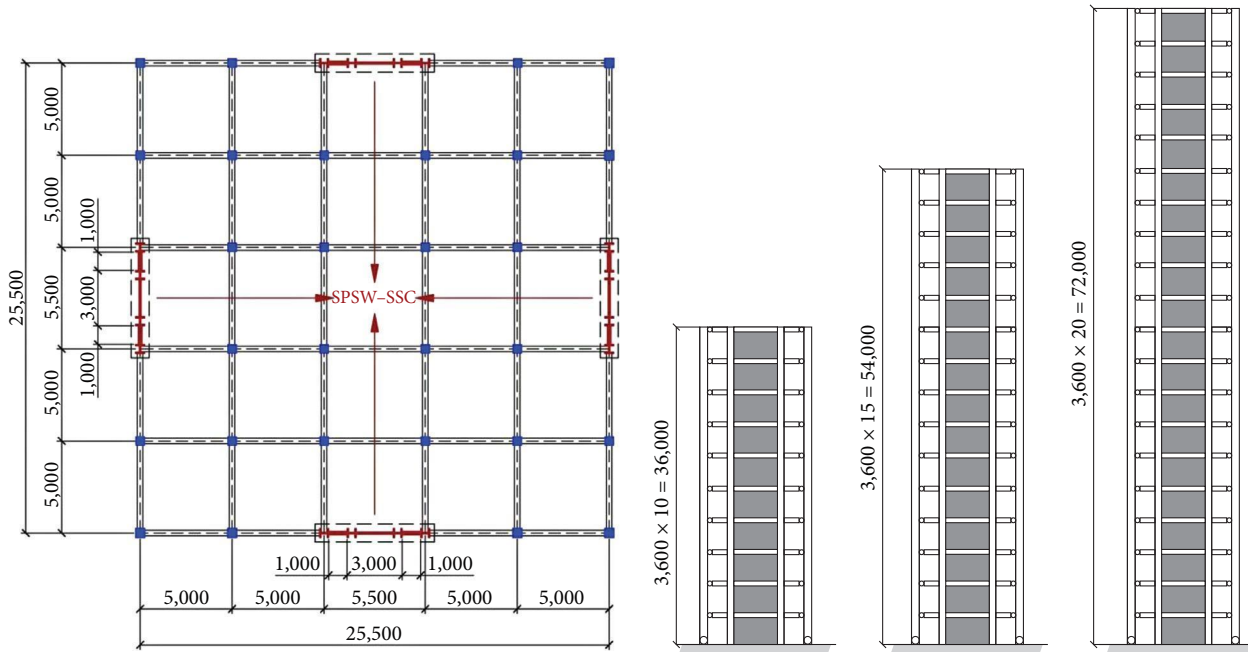

(a) (b)

FIGURE 8: Prototype structures of SPSW–SSC coupled system: (a) floor plan and (b) elevations.

$$M_{\mathrm{W}} = 2M_{\mathrm{VBE}} + \frac{L_{\mathrm{W}}}{2}\left(\sum_{i=1}^{n} F_{\mathrm{y}} H_i t_i \sin 2\alpha_i + \sum_{i=1}^{n} \frac{4}{L_{\mathrm{W}}} \mathrm{M}_{\mathrm{HBE},i} - 2\sum_{i=1}^{n} \mathrm{V}_{\mathrm{SCB},i}\right). \tag{22}$$

To choose the thickness of steel web plate of the SPSW, it is assumed that the story shear is totally resisted by the horizontal component of the tension field of the web plate. The thickness of the steel web plate can be calculated by the following equation:

$$\sum_{i=1}^{n} F_{\mathrm{w},i}^{\mathrm{D}} = \frac{1}{2} L_{\mathrm{W}} F_{\mathrm{y}} t_i \sin 2\alpha_i, \tag{23}$$

where $F_{\mathrm{w},i}^{\mathrm{D}}$ is the equivalent lateral force at the ith floor of SPSW; t_i is the thickness of the ith floor of steel web plates.

To ensure the plastic hinges occur at both ends of the HBE, the maximum bending moment must not occur at midspan. The distance measured from the maximum bending moment location to the left end of the beam at the ith floor ($\chi_{\mathrm{s},i}$) should be checked with Equation (24):

$$\chi_{\mathrm{s},i} = \frac{2M_{\mathrm{HBE},i}}{\omega_{\mathrm{V,HBE}i} L_{\mathrm{W}}} - \frac{L_{\mathrm{W}}}{2} \geq 0, \tag{24}$$

where $M_{\mathrm{HBE},i}$ is the bending moment transferred from HBE to VBE, $\omega_{\mathrm{V,HBE}i}$ is the vertical component of tension field at the ith floor. To make the compression-bending plastic hinge occur at the base of VBEs, the height of the maximum bending moment point (h_{s}) should be checked with Equation (25):

$$h_{\mathrm{s}} = \frac{H_1}{2} - \frac{M_{\mathrm{HBE},1} + M_{\mathrm{VBE}}}{\omega_{\mathrm{h,VBE1}} H_1} \leq 0, \tag{25}$$

where H_1 is the height of bottom story, $M_{\mathrm{HBE},1}$ is the bending moment transferred from HBE to VBE, M_{VBE} is the couple carried by VBE on both sides, and $\omega_{\mathrm{h,HBE1}}$ is the horizontal component of the tension field at the bottom story. Both HBEs and VBEs need to meet the check of compression-bending capacity, shear capacity, and moment of inertia.

3. Design of Prototype SPSW–SSC Coupled Systems

To verify the effectiveness of the proposed EBPD method and evaluate the seismic performance of the SPSW–SSC coupled system, 12 SPSW–SCC prototype structures with different CRs ranging from 0.3 to 0.6 and different story numbers of 10, 15, and 20 were designed based on the proposed EBPD method and the relevant Chinese code [25]. Each design case is identified by the story number and CR. For example, the identification W-10-0.3 represents a prototype SPSW–SSC system with 10 stories and a CR of 0.3. The story height of all prototype structures is 3.6 m. The design peak ground acceleration (PGA) is 0.2 g. The nominal yield strength of steel web plates is 235 MPa. Other steel members, including the SCB, VBE, HBE, and SSCs, adopt the shape steel with nominal yield strength of 345 MPa. The plan and elevation views of the prototype structures are shown in Figure 8. The symbols specifying the sectional dimensions of structural members are given in Figure 9. The design results of the structural members and the infill plate thickness for the

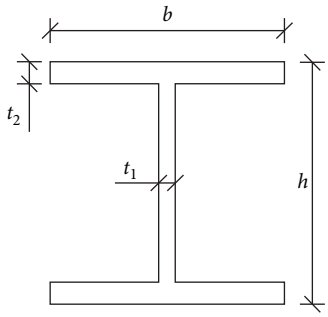

Figure 9: Cross-section of steel members.

Table 1: Sectional dimensions of steel members of W-10-0.3 (mm).

Steel members	h	b	t_1	t_2
SSC	200	100	4.5	7
VBE	400	300	10	16
SCB at 2nd–4th floors	110	74	5	9
SCB at 5th–8th floors	105	70	5	9
SCB at 9th-roof floors	100	68	5	8
HBE at 2nd–4th floors	200	150	7	10
HBE at 5th–8th floors	180	150	7	10
HBE at 9th–roof floors	150	150	7	10

Table 2: Steel infill plate thickness of W-10-0.3 (mm).

Floor level	t
1st–3rd stories	3.0
4th–7th stories	2.5
8th–10th stories	2.0

prototype case W-10-0.3 are given in Tables 1 and 2, as an example. It is noted all the dimensions of the steel members and the infill plates thickness are only for the numerical analysis. In practical design, these dimensions should be selected considering the availability of the steel product market.

4. Numerical Modeling and Verification

To obtain reliable analytical results while ensure computational efficiency, the proved-reliable program PERFORM-3D was used to establish the numerical models of all the prototype SPSW–SSC coupled structures. The accuracy and efficiency of the adopted modeling techniques were verified by the comparison between numerical and experimental results for a coupled SPSW system.

4.1. Numerical Modeling. The multilayer shell element was used to simulate the steel web plates of the SPSW-SCC system. SCBs, SSCs, and boundary frame members were simulated by the frame elements. Pinned connections were used to join the SCBs and the SSCs. Rigid connections were assigned between the SCBS and the VBEs. According to the designed ultimate yield mechanism, the moment M3 hinges were added to HBEs, shear V3 hinge was added to SCBs, and the PMM hinge added to the bottom of VBEs. The bases of SSCs were set pinned. The bilinear kinematic hardening model was adopted as the stress–strain relationship of steel, which also follows the Mises yield criterion. The elastic modulus and the Poisson ratio of the steel are 200 GPA and 0.3, respectively. Based on the preliminary stability analysis, the first buckling mode with a magnitude of 1/1,000 of the dimension of the steel web plate was defined as the initial imperfection of the model.

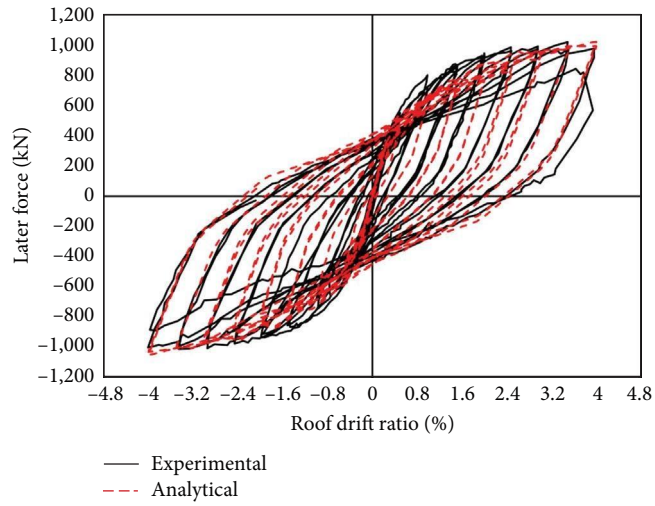

Figure 10: Comparison of experimental and analytical hysteresis curves.

4.2. Verification of Numerical Modeling. Since the experimental study on the SPSW–SSC system was not available in literature, the coupled SPSW was selected instead to provide experimental results for comparison with the simulation results to verify the accuracy and efficiency of the modeling techniques. The three-story coupled SPSW test model in the literature [33] was modeled and loaded in the exactly same way as reported to simulate the experimental results. The comparison of the simulated and experimental hysteresis curves is shown in Figure 10. The experimental peak lateral load and initial stiffness are slightly higher than the analytical results. The peak lateral load capacity in the positive loading direction is slightly lower than that in the negative loading direction, which is the same as the test results. In general, the simulation results agree very well with the test results. The error is within acceptable limits. The modeling techniques can be used to simulate the SPSW–SSC coupled system with adequate accuracy and efficiency.

5. Pushover Analysis

The pushover analysis was carried out to obtain the capacity curve with the monotonic increase of lateral displacement. The lateral force distribution pattern proposed by Chao et al. [27] was adopted to better reveal the base shear versus deformation characteristics of the SPSW–SSC coupled system into plastic stage. The base shear versus roof lateral drift ratio capacity curves of all three groups of prototype SPSW–SSC systems are plotted in Figure 11. The two critical events marked on the curves represent the yielding of half of

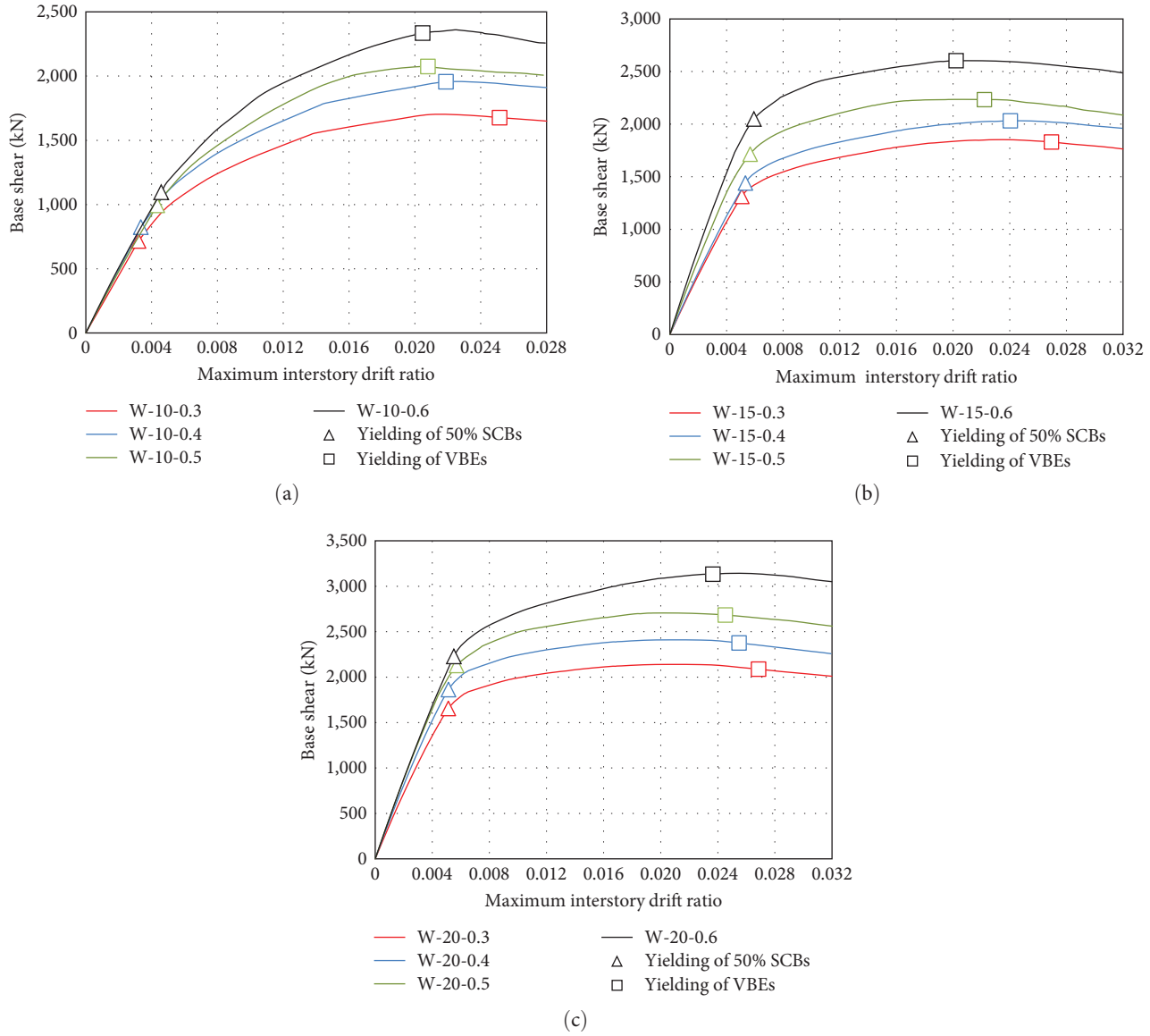

Figure 11: Pushover curves of structures: (a) W-10, (b) W-15, and (c) W-20.

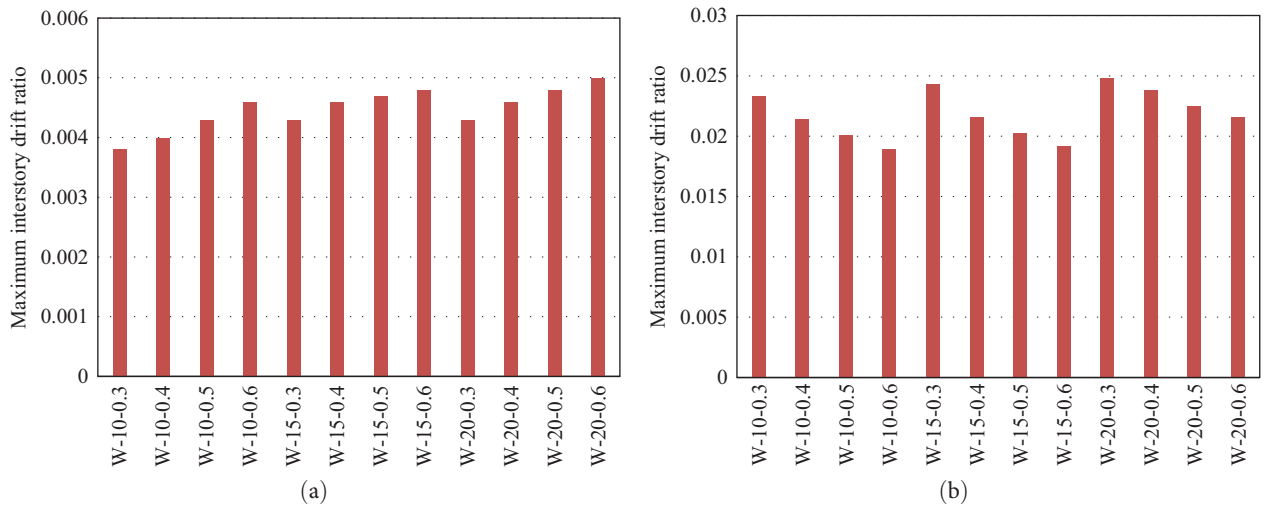

Figure 12: Maximal interstory drift ratio: (a) yielding of half of SCBs and (b) yielding of VBEs.

Table 3: Range of interstory drift ratios for different performance levels (PL).

LS	LS1	LS2	LS3	LS4	LS5
PL	No damage	Minor damage	Moderate damage	Serious damage	Near collapse
Interstory drift ratio	<1/650	1/650–1/400	1/400–1/200	1/200–1/100	1/100–1/50

Table 4: Ground motion records for IDA.

ID	Location	Magnitude	Station	PGA (g)	Duration (s)
USA00509	San Fernando	6.6	6,075 Park Drive, Wrightwood, CA: Gnd Fl	0.557	19.92
USA00867	Long Beach, California	6.5	Subway Terminal, Los Angeles, CA: Sub-bsmt	0.636	119.03
USA01555	Southeastern Alaska	7.6	Magnetic Obsv, Sitka, Alaska	0.699	55.28
USA00855	Puget Sound Washington	6.5	Federal Office Bldg, Seattle, Washington	0.321	74.13
USA02378	Coalinga	6.5	Parkfield, Cholame 2wa	0.437	60.00
USA00118	Borrego Mountain, California	6.7	Southern CA Edison, Nuclear Power Plant, San Onofre, CA	0.400	45.20
USA00730	San Fernando	6.6	5260 Wilshire Blvd, Los Angeles, CA: Roof	0.612	49.07
ROM00056	Vrancea, Romania	6.5	Muntele Rosu	0.310	67.28
USA00009	Kern County California	7.7	Pasadena, Caltech, Athenaeum, CA	0.298	77.28
Artificial 1	—	—	—	0.220	40.00
Artificial 2	—	—	—	0.220	40.00

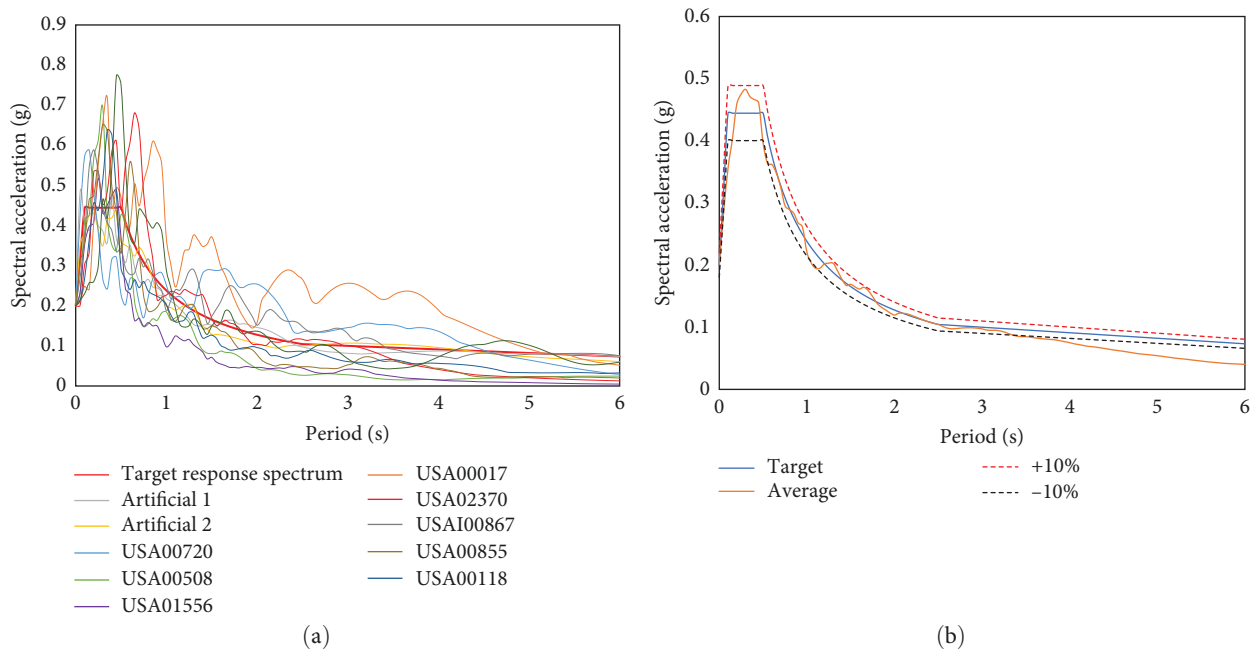

Figure 13: Response spectrum of selected ground motion records: (a) response spectrum of ground motions and (b) comparison of response spectrum.

SCBs and the yielding of the base of VBE of SPSW, respectively. The curves of SPSW–SCC systems with different story numbers show a similar trend. With the same story number, the larger the CR, the greater the lateral stiffness and peak lateral capacity. The maximum interstory drift ratio corresponding to the yielding of 50% SCBs increases with CR while that corresponding to the yielding of VBE decreases with CR. It is implied that using higher CR can enhance the lateral stiffness and strength while reducing the postyield deformation capacity, or the ductility of the SPSW–SSC system. The most obvious influence of story number can be found in the difference between the capacity curves of the 10-story prototype cases (Figure 11(a)) and those of other cases with 15 and 20 stories (Figures 11(b) and 11(c)). No matter what CR is used, the yielding of 50% SCBs of the W-10 cases does not bring the structure into a plastic plateau.

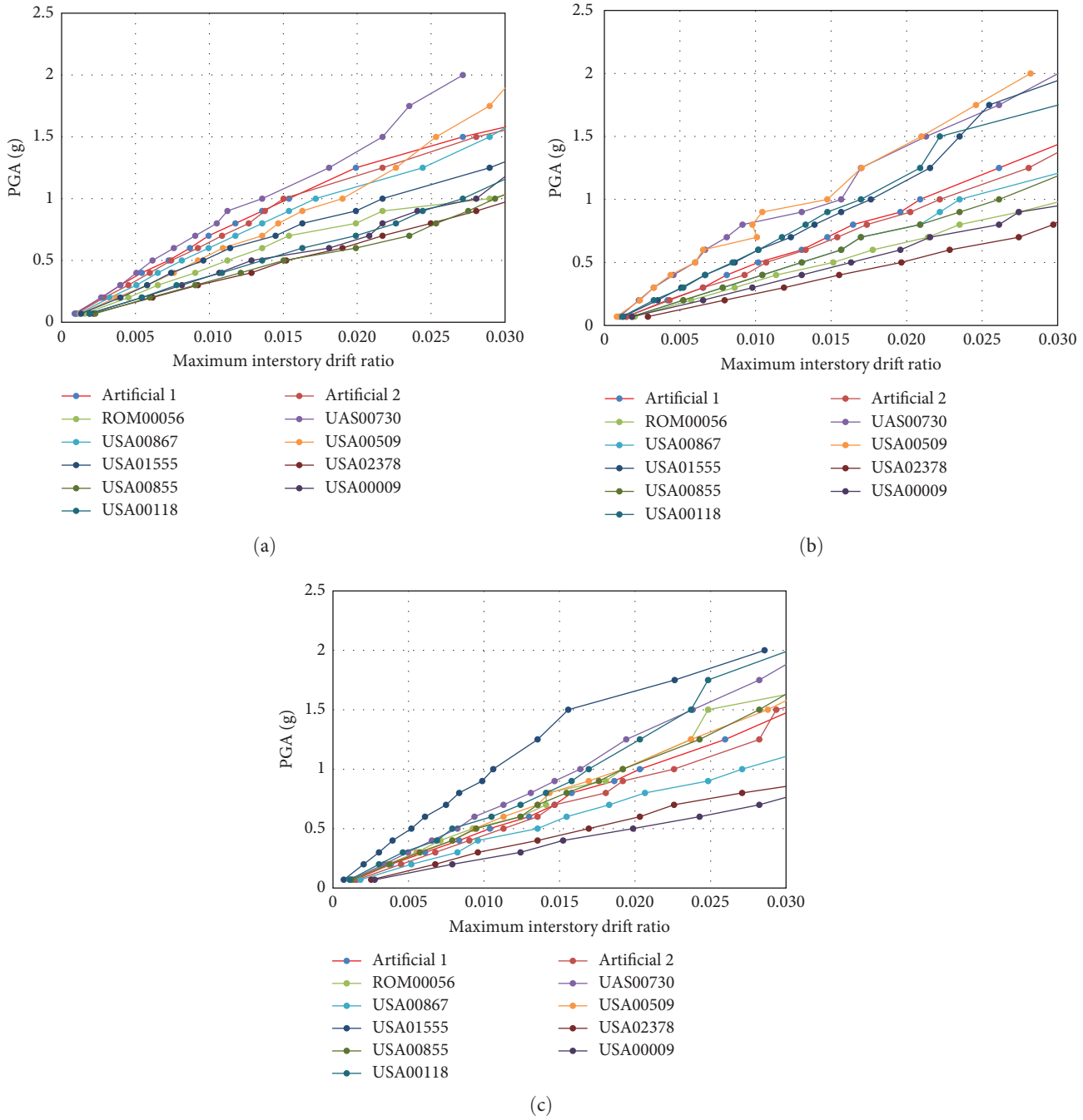

Figure 14: IDA curves of prototype cases: (a) W-10-0.4, (b) W-15-0.4, and (c) W-20-0.4.

The lateral load-carrying capacity of the coupled system continues to increase till the VBEs of the SPSW yield and then the capacity curves enter the plastic plateau. For the 15-story and 20-story prototype cases, the yielding of 50% SCBs indicates the "softening" of the structural system and the increase of lateral capacity is much slower than the lateral deformation, which is similar to the plastic plateau. Compared with the prototype cases of W-15 and W-20, the yielding of 50% SCBs of the W-10 cases occurs at a lateral interstory drift ratio about 0.004 rad, which is less than that of the W-15 and W-20 cases.

The maximum interstory drift ratios of all three groups of SPSW–SSC systems corresponding to the yielding of half of SCBs and the base of VBEs are shown in Figure 12. In Figure 12(a), all the maximum interstory drift ratios at yielding of 50% of SCBs are less than 1/200. When the base of VBEs of the SPSW yields, the maximum interstory drift ratios of all cases exceed 1/50 except for W-10-0.6 and W-15-0.6. Thus, before the yielding of the SPSW, the most of the SCBs have developed considerable postyield deformation and consumed a great deal of energy. It is also indicated that for the

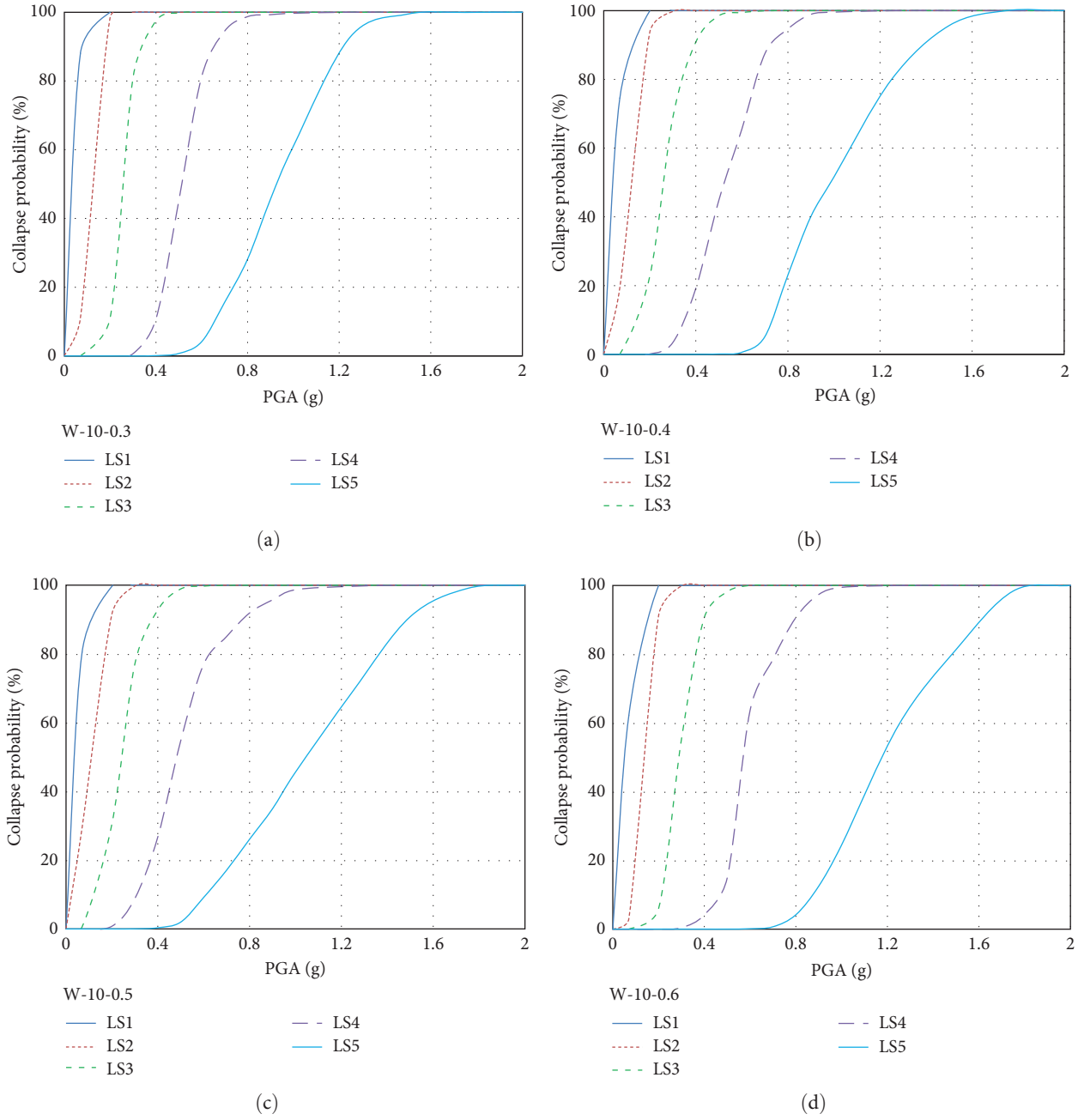

Figure 15: Continued.

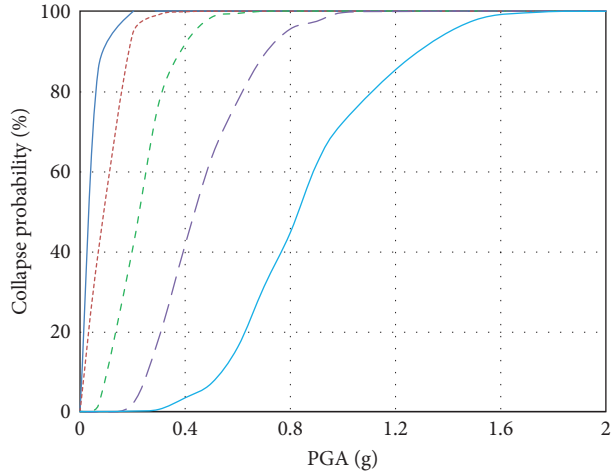

(e)

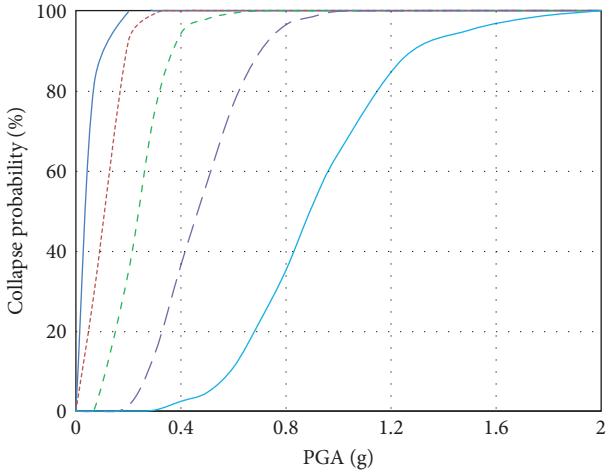

(f)

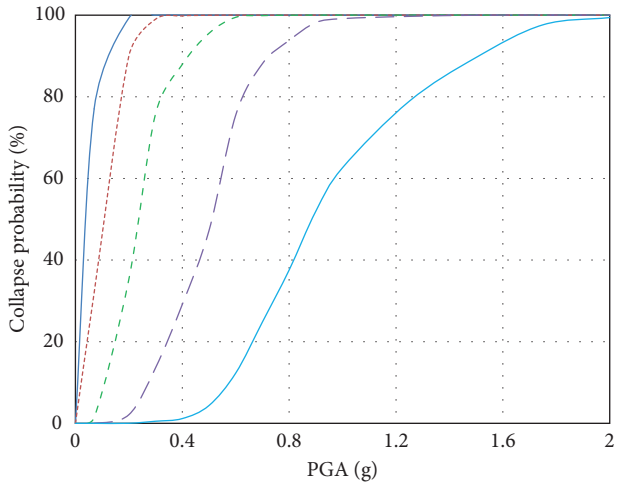

(g)

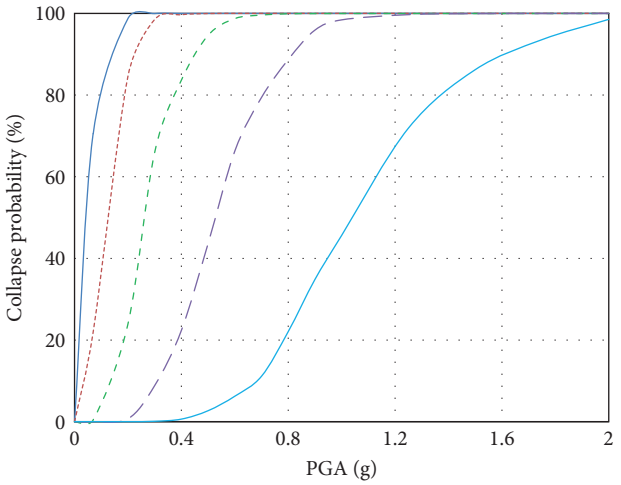

(h)

Figure 15: Continued.

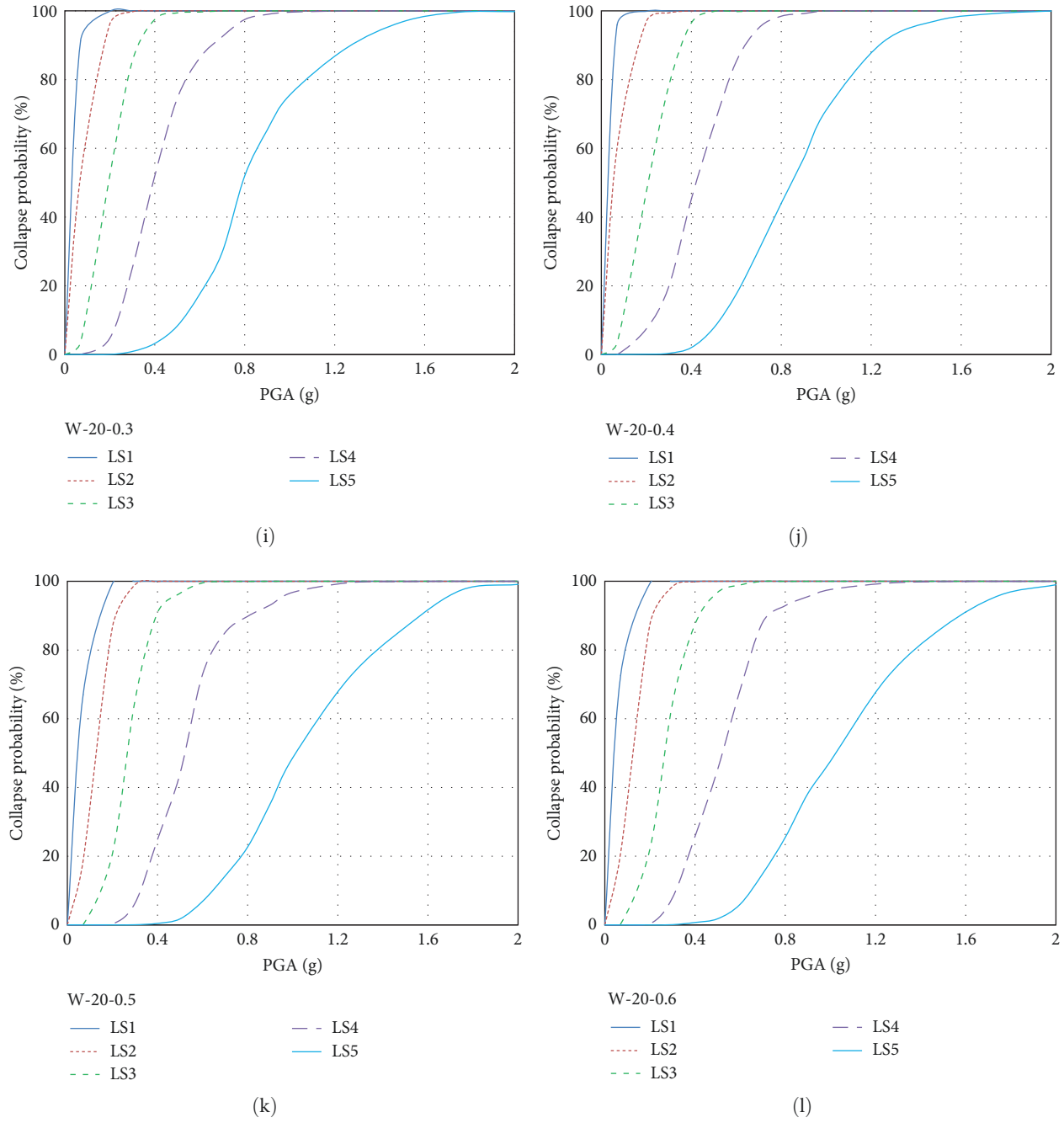

FIGURE 15: Seismic fragility curves of all prototype cases: (a) W-10-0.3, (b) W-10-0.4, (c) W-10-0.5, (d) W-10-0.6, (e) W-15-0.3, (f) W-15-0.4, (g) W-15-0.5, (h) W-15-0.6, (i) W-20-0.3, (j) W-20-0.4, (k) W-20-0.5, and (l) W-20-0.6.

realization of the performance objectives the selection of CR should avoid the upper bound of 0.6. For best material efficiency out of the coupling mechanism, the optimal number of stories for the SPSW–SSC coupled system should be more than 10 stories.

6. Seismic Fragility Analysis

All the SPSW–SSC prototype cases were further analyzed using the IDA method to reveal the damage development characteristics with the increase of earthquake excitation intensity [34–36]. Then, the seismic fragility curves of the SPSW–SSC systems were obtained based on the IDA results.

6.1. Intensity and Damage Measures. The PGA instead of the first-mode spectral acceleration Sa (T_1, 5%) was selected as the intensity measure (IM) since all the structures to be analyzed are high-rise and the influence of higher order modes cannot be ignored [37]. The interstory drift ratio was adopted as the damage measure (DM) to remain consistent with the design. The limit states (LS) of the SPSW–SSC coupled system corresponding to different performance levels (PL) were

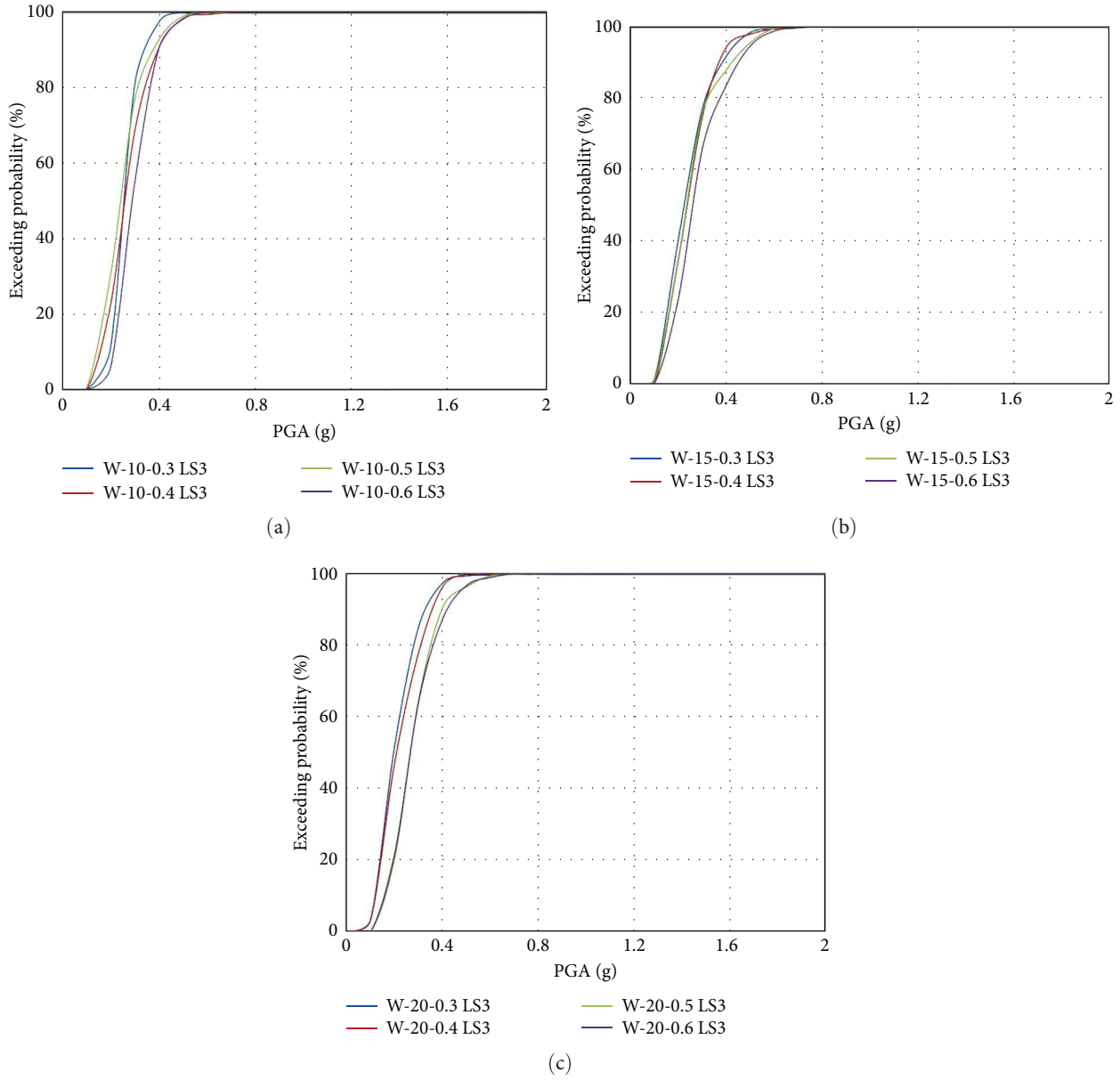

Figure 16: Seismic fragility curves for LS3: (a) W-10 prototype cases, (b) W-15 prototype cases, and (c) W-20 prototype cases.

quantified in terms of the interstory drift ratio [25, 31]. As listed in Table 3, the limit state LS1 is corresponding to all structural members in elastic state; LS2 corresponds to the yielding of some steel web plates; LS3 corresponds to yielding of half of SCBs; LS4 corresponds to yielding of HBEs of SPSW; and LS5 corresponds to yielding of VBEs of SPSW.

6.2. Input Ground Motions. Nine natural ground motions and two artificial waves were selected, as shown in Table 4. The acceleration response spectrum of the selected ground motion records and the target response spectrum are given in Figure 13(a). As demonstrated in Figure 13(b), the difference between the average response spectrum of the selected acceleration records response spectrum and the target response spectrum is within $\pm 10\%$. All the ground motion records were normalized and scaled to form a series of PGA ranging from 0.07 to 2.0 g. After 0.07 g PGA was analyzed, the next step analysis used 0.2 g. Then, the subsequent analysis steps adopted a constant PGA increment of 0.1 g until 2.0 g PGA was reached. It is noted that in the Chinese seismic design code [25], the PGA of 0.2 g corresponds to an earthquake with an exceedance probability of 10% in 50 years, while a PGA of 0.4 g corresponds to an earthquake with an exceedance probability of 2% in 50 years.

6.3. Seismic Fragility Analysis

6.3.1. Seismic Fragility Curves. Each prototype SPSW–SSC coupled system was analyzed using the selected suite of ground motion records following the IDA procedure. The multirecord IDA curves were obtained for each prototype case and those

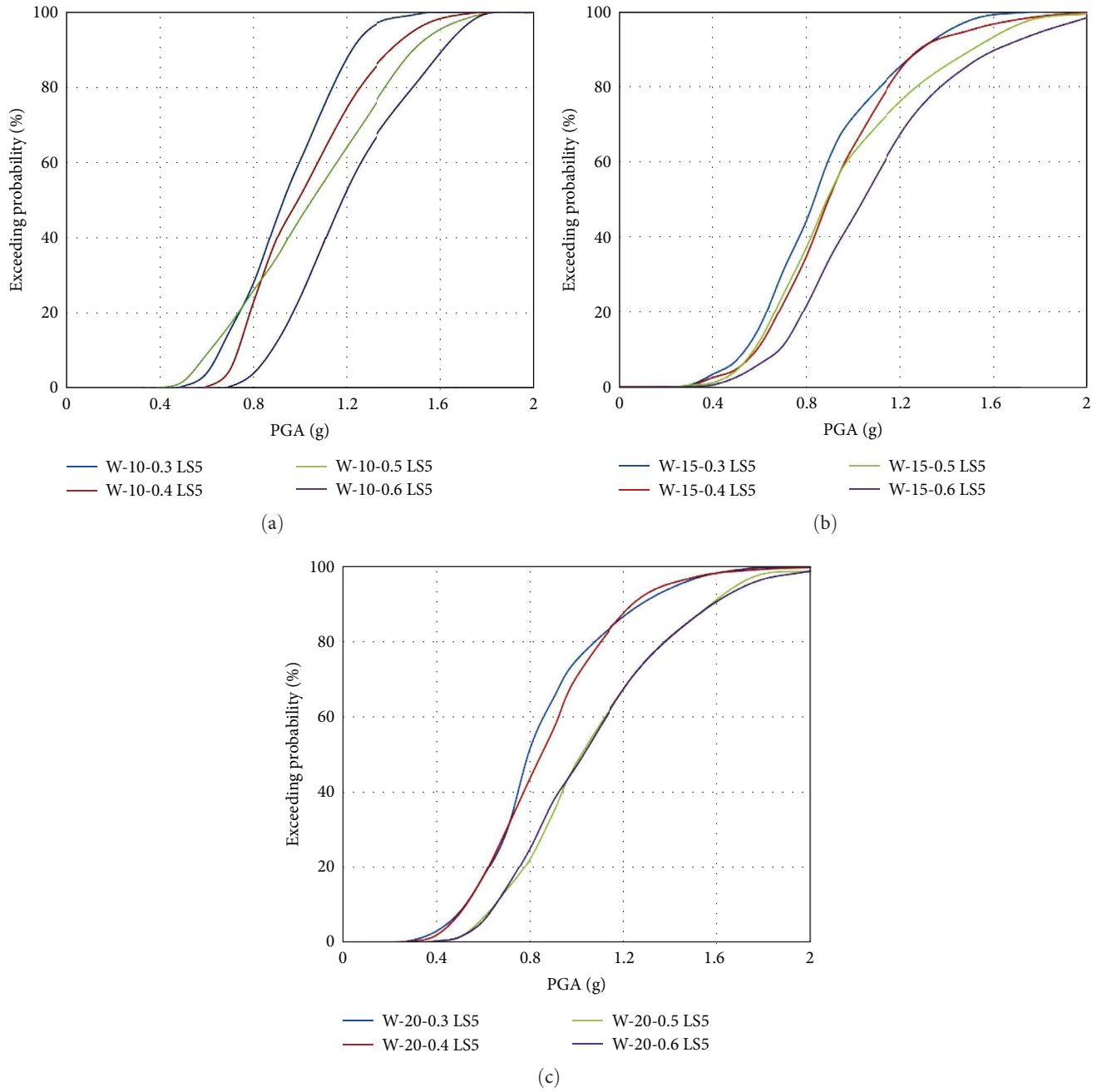

Figure 17: Seismic fragility curves for LS5: (a) W-10 prototype cases, (b) W-15 prototype cases, and (c) W-20 prototype cases.

of the prototype cases W-10-0.4, W-15-0.4, and W-20-0.4 are shown in Figure 14 as examples. The horizontal and vertical axes represent the maximum interstory drift ratio and PGA, respectively. These IDA curves were used to obtain the fragility curves reflecting the probability of exceeding the limit states of different performance levels quantified by the maximum interstory drift ratios, as indicated in Table 3.

The seismic fragility curves corresponding to all limit states of the SPSW–SSC prototype cases are plotted in Figure 15. The horizontal and vertical axes are PGA and exceeding probability, respectively. The fragility curve for the limit state LS5 of the W-20-0.6 case can be taken as an example, as shown in Figure 15(l). The vertical axis coordinate of the point on the curve corresponding to the PGA of 1.0 g is 47.61%, meaning when the PGA reaches 1.0 g, the damage limit state of W-20-0.6 has a probability of 47.6% to exceed the limit state of LS5 (near collapse). All fragility curves for the 12 prototype cases show similar trends. Along with the increase of severity of damage conditions from LS1 to LS5, the required increment of PGA to lead to 50% of exceeding probability increases significantly. Particularly, to exceed the ultimate limit state LS5 with 50% probability, the corresponding PGA is approximately 1.0 g for all prototype cases, implying the satisfactory collapse prevention capacity

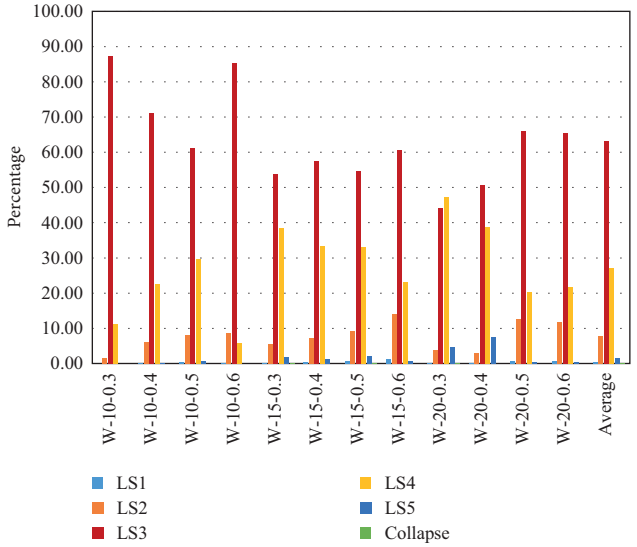

Figure 18: Damage probability of structure under moderate earthquake (PGA = 0.2 g).

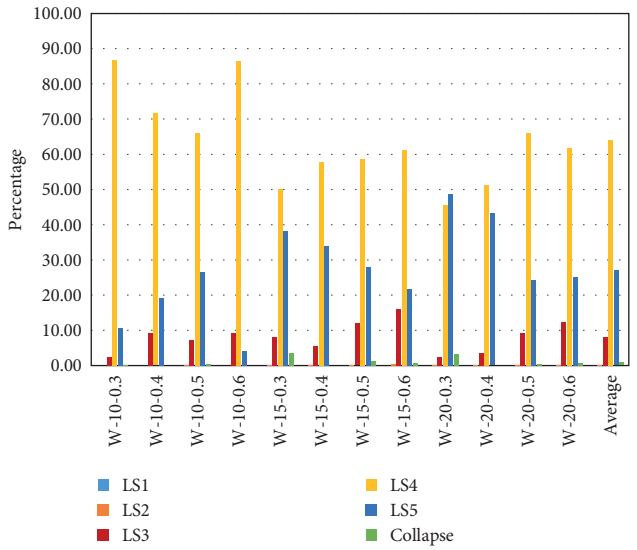

Figure 19: Damage probability of structures under rare earthquakes (PGA = 0.4 g).

of the SPSW–SSC coupled system. The limit state LS3 corresponding to the damage level characterized by the yielding of half of the total SCBs has a reasonable PGA approximately 0.4 g for 50% exceeding probability, indicating the SCBs can effectively be designed to serve as the energy dissipation elements under rare earthquake disasters.

Figures 16 and 17 demonstrate the seismic fragility curves corresponding to the key limit states of LS3 and LS5 for each group of prototype cases with the same story number. It can be seen that with the increase of CR, the PGA that leads to 50% of exceeding probability for each performance level also increases. For the 10-story prototype cases, the fragility curves corresponding to different CRs are also distinctive, as shown in Figures 16(a) and 17(a). For the 15-story prototype cases, as shown in Figures 16(b) and 17(b), the CRs 0.4 and 0.5 cause little difference to the fragility curves, indicating the low, medium, and high CR values are 0.2, 0.4, 0.5, and 0.6, respectively. For the prototype cases with 20 stories, the CRs of 0.5 and 0.6 can result in very close fragility curves with respect to LS3 and LS5, as can be seen in Figures 16(c) and 17(c), indicating that for 20-story prototype cases CRs between 0.5 and 0.6 can be regarded as high CR values.

6.3.2. Verification of Performance Objectives. The probabilities for the SPSW–SSC prototype systems reaching different limit states under moderate earthquakes (PGA = 0.2 g) and rare earthquakes (PGA = 0.4 g) are shown in Figures 18 and 19, respectively. Under moderate earthquakes, the average probability of the 12 prototype structures reaching LS3 is 64.1%, while that of reaching LS4 is 27.8%. Under rare earthquakes, the average probability for all prototype cases to reach LS4 is 64.0%, while that of reaching LS5 is 27.0%. The average probability of collapse is only 0.83%. According to the definitions of performance objectives, it is obvious that the design performance objectives for the SPSW–SSC coupled systems are fulfilled.

7. Summary and Conclusion

In this research program, the EBPD method was developed for the seismic design of the proposed SPSW–SSC coupled structural system. The EBPD method combines the energy-balance concept and the plastic design approach and can directly reflect the favorite plasticity development and distribution pattern determined by the coupling mechanism at the early design stage. In addition, the seismic base shear can be directly computed using the energy-balance-based approach without the iteration procedure if traditional method is used. Twelve prototype SPSW–SSC coupled systems considering various story numbers and CRs were designed and numerically modeled with PERFORM-3D. The numerical modeling method was verified by comparing the simulated results with the experimental ones obtained from the available literature. Then, the pushover analysis and IDA-based seismic fragility analysis with respect to five performance levels quantified by five limit states of the maximum interstory drift ratios were further conducted. The following conclusions can be made based on the numerical studies:

(i) According to the capacity curves obtained from the pushover analyses, for all the prototype cases, the maximum interstory drift ratio corresponding to the yielding of half of the SCBs increases with the CR, while that corresponding to the yielding of the VBEs of the SPSW decreases. This indicates that the higher the CR the poorer the postyield deformation capacity. With the increase of CR, the lateral load capacity of the prototype cases increases too.

(ii) The capacity curves also show that for the prototype cases with the story number of 10, the maximum interstory drift ratios are close to 0.004 rad, which is less than that for the prototype cases with the story numbers of 15 and 20; after the yielding of half of

the SCBs, the capacity curves continue to ascend till the yielding of the VBEs of the SPSW. However, for the prototype cases with the story numbers of 15 and 20, the capacity curves enter the plastic plateau after the yielding of half of the SCBs. It is, thus, suggested the SPSW–SSC coupled systems with 15 and 20 stories exhibit better coupling mechanism than those with 10 stories.

(iii) According to the seismic fragility curves obtained from the IDA, along with the increase of severity of damage conditions from LS1 to LS5, the required increment of PGA to lead to 50% of exceeding probability increases significantly. Particularly, to exceed the ultimate limit state LS5 (near collapse) with 50% probability, the corresponding PGA is approximately 1.0 g for all prototype cases, implying the satisfactory collapse prevention capacity of the SPSW–SSC coupled system. The limit state LS3 corresponding to the performance level characterized by the yielding of half of the total SCBs has a reasonable PGA approximately 0.4 g for 50% exceeding probability, indicating the SCBs can effectively be designed to serve as the energy dissipation elements under rare earthquake disasters.

(iv) Under moderate earthquakes, the average probability of the 12 prototype cases in LS3 and LS4 are 64.04% and 27.74%, respectively. Under rare earthquakes, the average probability of the 12 prototype cases in LS4 and LS5 are 63.99% and 26.99%, respectively. The average probability of collapse is only 0.83%. The performance objective of collapse prevention under rare earthquakes can be satisfied.

Data Availability

The authors confirm that the data supporting the findings of this study are available within the article.

Conflicts of Interest

The authors declare that they have no conflicts of interest.

Authors' Contributions

Y. T. Wu contributed to conceptualization, funding acquisition, project administration, analysis, and writing—original draft. Auzhou Liu contributed to resources, methodology, analysis, and data transaction. Jiazheng Zhao contributed to analysis and data transaction. Bo Zhang contributed to conceptualization and writing—review and editing.

Acknowledgments

This research project is financially sponsored by the National Natural Science Foundation of China (Grant No. 51978101) and the China State Construction Science and Technology Plans (Grant No. CSCEC-2020-Z-32). The authors would like to express their sincere thanks and appreciation to the supporting agencies of this project.

References

[1] Y. Takahashi, T. Takemoto, and M. Tagaki, "Experimental study on thin steel shear walls and particular bracing under alternative horizontal load," International Association for Bridge and Structural Engineering (IABSE), Zurich, Switzerland, pp. 185–191, 1973, Preliminary Report, Symposium on Resistance and Ultimate Deformability of Structures Acted on by Well-Defined Repeated Loads.

[2] A. Astaneh-Asl, "Seismic behavior and design of steel shear walls," Structural Steel Education Council, Steel TIPS report, 2001.

[3] R. G. Driver, G. L. Kulak, D. J. L. Kennedy, and A. E. Elwi, "Cyclic test of four-story steel plate shear wall," *Journal of Structural Engineering*, vol. 124, no. 2, pp. 112–120, 1998.

[4] M. Elgaaly, "Thin steel plate shear walls behavior and analysis," *Thin-Walled Structures*, vol. 32, no. 1–3, pp. 151–180, 1998.

[5] A. S. Lubell, H. G. L. Prion, C. E. Ventura, and M. Rezai, "Unstiffened steel plate shear wall performance under cyclic loading," *Journal of Structural Engineering*, vol. 126, no. 4, pp. 453–460, 2000.

[6] T. Zirakian and J. Zhang, "Structural performance of unstiffened low yield point steel plate shear walls," *Journal of Constructional Steel Research*, vol. 112, pp. 40–53, 2015.

[7] M. G. Azandariani, M. Gholhaki, and M. A. Kafi, "Experimental and numerical investigation of low-yield-strength (LYS) steel plate shear walls under cyclic loading," *Engineering Structures*, vol. 203, Article ID 109866, 2020.

[8] P. M. Clayton, J. W. Berman, and L. N. Lowes, "Seismic performance of self-centering steel plate shear walls with beam-only-connected web plates," *Journal of Constructional Steel Research*, vol. 106, pp. 198–208, 2015.

[9] A. Farzampour, J. A. Laman, and M. Mofid, "Behavior prediction of corrugated steel plate shear walls with openings," *Journal of Constructional Steel Research*, vol. 114, pp. 258–268, 2015.

[10] D. Vian, M. Bruneau, K. C. Tsai, and Y. C. Lin, "Special perforated steel plate shear walls with reduced beam section anchor beams. I: experimental investigation," *Journal of Structural Engineering*, vol. 135, no. 3, pp. 211–220, 2009.

[11] A. G. Azandariani, M. Gholhaki, and M. G. Azandariani, "Assessment of damage index and seismic performance of steel plate shear wall (SPSW) system," *Journal of Constructional Steel Research*, vol. 191, Article ID 107157, 2022.

[12] K. Oh, H. Ha, B. Jo, and K. Lee, "An analytical study on structural performance evaluation of coupled steel plate shear wall systems," *International Journal of Steel Structures*, vol. 19, no. 1, pp. 1–13, 2019.

[13] D. J. Borello and L. A. Fahnestock, "Behavior and mechanisms of steel plate shear walls with coupling," *Journal of Constructional Steel Research*, vol. 74, pp. 8–16, 2012.

[14] M. Wang, D. J. Borello, and L. A. Fahnestock, "Boundary frame contribution in coupled and uncoupled steel plate shear walls," *Earthquake Engineering & Structural Dynamics*, vol. 46, no. 14, pp. 2355–2380, 2017.

[15] A. Pavir and B. Shekastehband, "Hysteretic behavior of coupled steel plate shear walls," *Journal of Constructional Steel Research*, vol. 133, pp. 19–35, 2017.

[16] S. El-Tawil, K. A. Harries, P. J. Fortney, B. M. Shahrooz, and Y. Kurama, "Seismic design of hybrid coupled wall systems: state of the art," *Journal of Structural Engineering*, vol. 136, no. 7, pp. 755–769, 2010.

[17] A. Zona, H. Degée, G. Leoni, and A. Dall'Asta, "Ductile design of innovative steel and concrete hybrid coupled walls," *Journal of Constructional Steel Research*, vol. 117, pp. 204–213, 2016.

[18] R. Das, R. Steensels, D. Dragan, B. Vandoren, and H. Degée, "Characterization and optimization of a steel beam to RC wall connection for use in innovative hybrid coupled wall systems," *Structures*, vol. 23, pp. 111–125, 2020.

[19] M. Salameh, M. Shayanfar, and M. A. Barkhordari, "Seismic displacements and behaviour factors assessment of an innovative steel and concrete hybrid coupled shear wall system," *Structures*, vol. 34, pp. 20–41, 2021.

[20] S. Leelataviwat, S. C. Goel, and B. Stojadinovic, "Toward performance-based seismic design of structures," *Earthquake Spectra*, vol. 15, no. 3, pp. 435–461, 1999.

[21] S. Leelataviwat, W. Saewon, and S. C. Goel, "Application of energy balance concept in seismic evaluation of structures," *Journal of Structural Engineering*, vol. 135, no. 2, pp. 113–121, 2009.

[22] S. C. Goel, W.-C. Liao, M. R. Bayat, and S.-H. Chao, "Performance-based plastic design (PBPD) method for earthquake-resistant structures: an overview," *The Structural Design of Tall and Special Buildings*, vol. 19, no. 1-2, pp. 115–137, 2010.

[23] M. S. Gorji and J. J. R. Cheng, "Plastic analysis and performance-based design of coupled steel plate shear walls," *Engineering Structures*, vol. 166, pp. 472–484, 2018.

[24] B. Zhang, Y. Wu, Q. Zhou, J. Bai, and Y.-B. Yang, "Energy-balance based plastic design and analysis of hybrid coupled wall system," *Structures*, vol. 33, pp. 4096–4111, 2021.

[25] M. Gholhaki, G. Pachideh, and A. Javahertarash, "Capacity spectrum of SPSW using pushover and energy method without need for calculation of target point," *Structures*, vol. 26, pp. 516–523, 2020.

[26] GB 50011-2010, *Code for Seismic Design of Buildings*, China Architecture & Building Press, Beijing, 2010.

[27] S.-H. Chao, S. C. Goel, and S.-S. Lee, "A seismic design lateral force distribution based on inelastic state of structures," *Earthquake Spectra*, vol. 23, no. 3, pp. 547–569, 2007.

[28] R. Park, "Ductility evaluation from laboratory and analytical testing," in *Proceedings of the 9th World Conference on Earthquakes Engineering*, WCEE, Japan, 1988.

[29] A. K. Chopra and R. K. Goel, "Capacity-demand-diagram methods for estimating seismic deformation of inelastic structures: SDF systems," Report No. PEER-1999/02, PEER, UC Berkeley, 1999.

[30] H. M. Dwairi, M. J. Kowalsky, and J. M. Nau, "Equivalent damping in support of direct displacement-based design," *Journal of Earthquake Engineering*, vol. 11, no. 4, pp. 512–530, 2007.

[31] G. M. Safari, "Design of steel plate shear wall systems with explicit consideration of drift demands and frame action," University of Alberta, Alberta, Canada, Doctoral Dissertation, 2017.

[32] ANSI/AISC 341-16, *Seismic Provisions for Structural Steel Buildings*, American Institute of Steel Construction, Chicago, 2016.

[33] D. J. Borello, "Behavior and large-scale experimental testing of steel plates shear walls with coupling," University of Illinois at Urbana-Champaign, Illinois, USA, Doctoral Dissertation, 2014.

[34] Y. Ma, Z. Wu, Z. Liu, M. Zhang, and M. Aibaidula, "Seismic fragility analysis of aqueduct structural systems based on G-PCM method," *Sustainability*, vol. 14, no. 20, Article ID 13161, 2022.

[35] C. Liu, D. Fang, L. Zhao, and J. Zhou, "Seismic fragility estimates of steel diagrid structure with performance-based tests for high-rise buildings," *Journal of Building Engineering*, vol. 52, Article ID 104459, 2022.

[36] C. Liu, D. Fang, and Z. Yan, "Seismic fragility analysis of base isolated structure subjected to near-fault ground motions," *Periodica Polytechnica Civil Engineering*, vol. 65, no. 3, pp. 768–783, 2020.

[37] D. Vamvatsikos and C. A. Cornell, "Incremental dynamic analysis," *Earthquake Engineering & Structural Dynamics*, vol. 31, no. 3, pp. 491–514, 2002.